DOI: 10.1002/ejic.201000166

Eu^{III}-Doping of Lamellar Bilayer and Amorphous Mono-Amide Cross-Linked Alkyl/Siloxane Hybrids

Silvia C. Nunes,[a] José Planelles-Aragó,[b,c] Rute A. S. Ferreira,[b] Luis D. Carlos,*[b] and Verónica de Zea Bermudez*[a]

Keywords: Organic–inorganic hybrid composites / Sol–gel processes / Luminescence / Europium

Two structurally different but chemically similar families of alkyl/siloxane mono-amidosil hosts, represented by m-A(x) [where x = 14 or 8 represents the number of CH_2 groups of the pendant alkyl chains directly bonded to the carbonyl group of the amide cross-link] have been doped with a wide range of concentrations of $Eu(CF_3SO_3)_3$. Mono-amidosils m-$A(x)_nEu(CF_3SO_3)_3$ with $n \geq 10$ (where n is the molar ratio of carbonyl groups per Eu^{3+} ion) have been analyzed. The m-$A(8)_nEu(CF_3SO_3)_3$ mono-amidosils are transparent and amorphous films, in which the alkyl chains adopt *gauche* conformations. In contrast, the m-$A(14)_nEu(CF_3SO_3)_3$ mono-amidosils are solid powders; here the lamellar bilayer hierarchical structure of m-A(14) coexists with a new lamellar phase in which the Eu^{3+} ions are bonded to carbonyl oxygen atoms of the amide groups. At n = 10 the hydrogen-bonded associations formed are highly ordered and considerably stronger than those found in the less concentrated hybrids and in the nondoped matrices. "Free" and weakly coordinated triflate ions occur in all the mono-amidosil samples. The hybrids are white light emitters (maximum quantum yield: 0.08 ± 0.01), presenting a broad emission band in the blue/purplish-blue spectral region (ascribed to the hybrid host) superimposed on the $^5D_0 \rightarrow {}^7F_{0-4}$ Eu^{3+} intra-$4f^6$ transitions. Two Eu^{3+} local coordination sites (named A and B) have been discerned in both systems. Site A is attributed to weakly coordinated $Eu^{3+}/CF_3SO_3^-$ ion pairs, whereas site B involves Eu^{3+} coordination to the oxygen atoms of the C=O groups, of the $CF_3SO_3^-$ ions and of the water molecules. For site B, the long-range order of the hybrid host induces distinct features in the energy of the $^5D_0 \rightarrow {}^7F_{0-4}$ transitions, the $^5D_0$ lifetime and the degree of covalency of the Eu^{3+}–first-ligand bonds.

1. Introduction

The mild sol–gel technique[1] is a versatile chemical synthetic route that permits the production of silica-based organic–inorganic hybrid materials[2] with potential applications in many fields.[1–3] A significant number of innovative and advanced organic–inorganic hybrids combining the interesting properties of organic materials (e.g., elastomeric nature) with the attractive features of an inorganic silica framework (e.g., thermal and dimensional stability) have been synthesized in the past years. Electrical, optical or structural properties can be tailored by controlling the chemical nature and reactions of the components. More recently, a new approach, which corresponds to the structuring of hybrid networks, has been explored.[4–9] This topic is considered to be one of the most challenging tasks of the sol–gel strategy, because the hybrids produced by means of the classical procedures are typically amorphous and featureless solids. Great efforts have been made in the last few years with the purpose of structuring and shaping these materials over multiple-length scales through the combination of sol–gel reactions with self-assembly routes. The nanostructure, degree of organization, complexity, levels of hierarchy and properties of such materials depend critically on the experimental conditions (e.g., temperature, pH, type of catalyst, type of solvent and water content). However, the chemical nature of the organic and inorganic components and the synergy created between them play a key role as well.

The extraordinary ability of silsesquioxanes {M_3-Si-$(CH_2)_3$-Y-R′-Y-$(CH_2)_3$-Si-M_3, where M = OR, Y = urea [-NHC(=O)NH-] group and R, R′ = organic groups} to self-assemble into a wide variety of tuneable morphologies has been extensively explored.[10] Organosilanes {R′-Y′-Si-M_3, where M = OR or Cl and Y′ = (-CH_2-)[11–14] or amide [-NHC(=O)NH-][15] groups}, a series of much simpler molecules, which exhibit the same type of phenomenon, have been considerably less investigated. In these two classes of hybrid materials, self-assembly relies on the establishment of weak interactions: hydrophobic (i.e., van der Waals) in-

[a] Department of Chemistry and CQ-VR, University of Trás-os-Montes e Alto Douro, 5001-801 Vila Real, Portugal
[b] Department of Physics, CICECO, University of Aveiro, 3810-193 Aveiro, Portugal
E-mail: lcarlos@ua.pt
vbermude@utad.pt
[c] Departamento de Química Inorgânica y Orgânica, Universitat Jaume I, Avda. Sos Baynat s/n, 12071, Castellón, Spain

Supporting information for this article is available on the WWW under http://dx.doi.org/10.1002/ejic.201000166.

teractions and/or π–π interactions between the R′ groups and hydrogen bonds between the cross-links (Y or Y′ = amide groups). In this context, we reported the first example of a photoluminescent lamellar bilayer hierarchically structured amide cross-linked alkyl/siloxane hybrid [*mono-amidosil*, m-A(14)],[15] in which these two types of interactions determine the emergence of a thermally actuated photoluminescence memory effect induced by a reversible order–disorder phase transition of the alkyl chains. In this material, the photoluminescence exhibits a unique nanoscopic nature.

The few known organized hybrid materials doped with lanthanide ions have been recently reviewed.[16] Among the works that were published subsequently,[17,18] it is of particular interest to refer to the synthesis of the first photoluminescent Eu^{3+}-doped lamellar polysilsesquioxanes self-templated through a hydrogen-bonding array.[19] In the present work, we have incorporated for the first time Eu^{3+} ions into two chemically similar but structurally different mono-amidosil host matrices, m-A(x) with x = 8 and 14, where x represents the number of CH_2 groups directly bonded to the carbonyl group of the amide cross-link (Scheme 1). As stated above, m-A(14) is a highly organized lamellar-type material,[15] whereas m-A(8) (in contrast) is entirely amorphous.[20] Our primary goal has been to determine the structural modifications resulting from the addition of increasing amounts of the guest lanthanide ions to the two hybrid host frameworks. The ultimate objective of this paper is to address the influence of the structure of the two mono-amidosil host matrices (with long-range order vs. short-range order) on their photoluminescence features by using Eu^{3+} ion as a local probe.

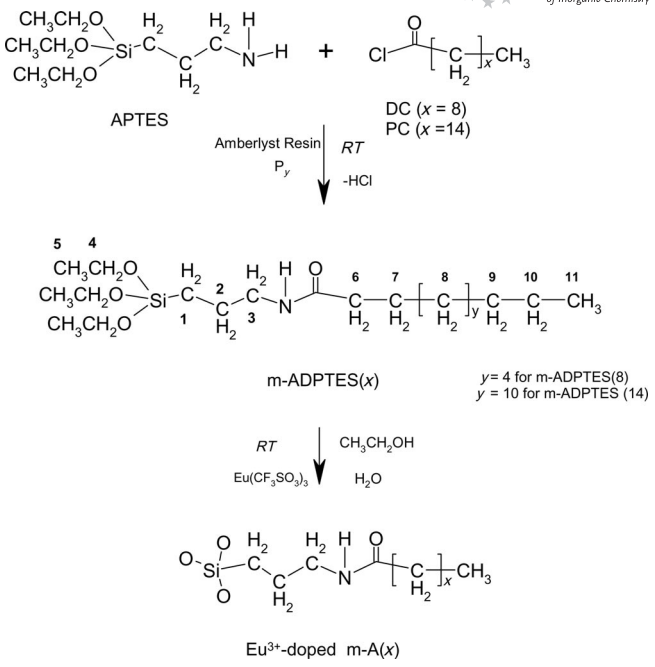

Scheme 1. Synthetic procedure for the m-A(x)$_n$Eu(CF_3SO_3)$_3$ mono-amidosils.

2. Results and Discussion

2.1. Synthesis of the Eu^{3+}-Doped m-A(x) Mono-Amidosils

The Eu^{3+}-doped m-A(x) mono-amidosils (x = 14 and 8) were prepared according to the method we have described in detail elsewhere.[15,20] The first stage of the synthetic procedure involved the formation of an amide cross-link between the Cl group of decanoyl chloride [Cl–C(=O)–$(CH_2)_8$-CH_3, DC, Aldrich] or palmitoyl chloride [Cl–C(=O)–$(CH_2)_{14}$-CH_3, PC, Aldrich] and the NH_2 group of 3-aminopropyltriethoxysilane [$(CH_3CH_2O)_3Si(CH_2)_3NH_2$, APTES, Fluka], in the presence of tetrahydrofuran (THF, Riedel-de-Haen), pyridine (Py, Aldrich) and Amberlyst A-21 Ion-Exchange Resin (Aldrich), to yield the organic–inorganic hybrid precursors designated as mono-amidepropyltriethoxysilanes [$(CH_3CH_2O)_3$–Si–$(CH_2)_3$–NH–C(=O)–$(CH_2)_x$–CH_3, m-ADPTES(x)] (Scheme 1).

In the second stage of the synthetic procedure, a mixture of ethanol (CH_3CH_2OH, Merck) and doubly distilled water was added to m-ADPTES(x) to promote the hydrolysis and condensation reactions characteristic of the sol–gel process, followed by the incorporation of europium triflate [$Eu(CF_3SO_3)_3$, Aldrich] (Scheme 1). While the Eu^{3+}-doped m-A(8) materials were obtained as transparent, rigid monoliths with a yellowish hue, the Eu^{3+}-doped m-A(14) hybrids were produced as white powders. The two series of samples have been represented by the notation m-A(x)$_n$Eu(CF_3SO_3)$_3$, where n is the molar ratio of amide carbonyl groups per Eu^{3+} ion. Additional details of the synthesis of the Eu^{3+}-doped m-A(x) mono-amidosils have been collected in Table S1. The results of the elemental analysis performed on the m-A(14)$_n$Eu(CF_3SO_3)$_3$ samples have also been included in Table S1. These data show that there is a reasonably good agreement between the theoretical and experimental Eu^{3+} concentrations in the m-A(14)-based mono-amidosils with $n \geq 20$. The only deviation worth mentioning is found in the case of the m-A(14)$_{10}$Eu(CF_3SO_3)$_3$ material, in which the real concentration of Eu^{3+} is significantly lower than the theoretical one. However, this was an expected result, considering the existence of free salt in this sample, as it will be demonstrated in the next section.

2.2. Structure and Thermal Behaviour of the Mono-Amidosils

Table 1 shows the position (δ) and assignment[12,15,21–23] of the resonance peaks of the ^{13}C CP/MAS and ^{29}Si MAS NMR spectra of representative samples of the m-A(14)$_n$-Eu(CF_3SO_3)$_3$ mono-amidosil family (Figures S1a and S1b).

The ^{13}C CP/MAS spectra of the Eu^{3+}-doped m-A(14) mono-amidosils represented in Figure S1(a) are dominated by a prominent peak centred around 34 ppm, due to the resonance of the C^8 carbon atoms (Scheme 1 and Table 1) and characteristic of highly ordered alkyl chains in *all-trans* zigzag conformations.[11,12a,24–26] Comparison of the other resonances present in these ^{13}C CP/MAS spectra [Figure S1(a), Scheme 1 and Table 1] with those reported earlier

Table 1. ^{13}C CP/MAS and ^{29}Si MAS NMR spectroscopic data of the m-A(14)$_n$Eu(CF$_3$SO$_3$)$_3$ mono-amidosils. R = $CH_3(CH_2)_{14}C(=O)NH–(CH_2)_3$- and c (polycondensation degree) = $1/3(\%T^1 + 2\%T^2 + 3\%T^3) \times 100$.

^{13}C CP/MAS			
	δ (ppm)		Assignment[12,15,21–23]
$n = \infty$[15]	$n = 200$	$n = 10$	
174	173	174	C^{12}
42	43	43	C^3
36	36	37	C^6
34	34	34	C^9
32	33	33	C^8 *trans*
26	26	26	C^7
24	24	25	C^2/C^{10}
14	15	14	C^{11}
11	12	10	C^1
^{29}Si MAS			
	δ (ppm) (% integrated area)		Assignment
$n = \infty$[15]	$n = 200$	$n = 10$	
–49.5 (8.5)	–47.8 (4.5)	–50.0 (6.8)	T^1
–57.8 (59.9)	–58.1 (59.1)	–60.0 (35.5)	T^2
–67.0 (31.6)	–66.9 (36.1)	–65.8 (57.6)	T^3
74	77	83	c
[a]	[b]	[c]	

[a] Empirical formula: R–Si(OSi)$_{0.8}$(OH)$_{1.1}$. [b] Empirical formula: R–Si(OSi)$_{1.1}$(OH)$_{0.7}$. [c] Empirical formula: R–Si(OSi)$_{1.2}$(OH)$_{0.5}$.

for the m-ADPTES(14) precursor[15] reveals that no cleavage of the functional groups of the m-ADPTES(14) precursor molecule (i.e., alkyl and propyl chains and amide cross-links) occurred during the second stage of the synthesis. The absence of peaks associated with the resonance of the ethoxy carbon atoms in the ^{13}C CP/MAS spectra of the m-A(14)$_n$Eu(CF$_3$SO$_3$)$_3$ samples indicates that the hydrolysis reaction was complete.[15]

The ^{29}Si MAS NMR spectra of the m-A(14)$_n$Eu(CF$_3$SO$_3$)$_3$ mono-amidosils exhibit three signals, assigned to the T^1 [CH_2-Si(OSi)(OH)$_2$], T^2 [CH_2-Si(OSi)$_2$(OH)] and T^3 [CH_2-Si(OSi)$_3$] sites, respectively [Figure S1(b) and Table 1]. The absence of T^0 sites in these spectra proves that, although the condensation reactions did not proceed to completion, no precursor was left unreacted. Moreover, the absence of Q-type sites (SiO_4 units) in Figure S1(b) is another piece of evidence that no cleavage of the Si–C bonds occurred. The relative proportion of the three silicon sites found in the m-A(14)-based samples examined demonstrates that T^2 and T^3 are the dominant environments (Table 1). The value of c calculated for the m-A(14)$_{200}$Eu(CF$_3$SO$_3$)$_3$ sample (77%), which is practically identical to that of the nondoped hybrid m-A(14) matrix (Table 1),[15] suggests the formation of a 2D siloxane network. The empirical formulas deduced from these data show that a small number of hydroxy groups stay bonded to the silicon atoms in both doped mono-amidosils (Table 1).

The XRD patterns of the Eu(CF$_3$SO$_3$)$_3$-doped m-A(14)-based mono-amidosils in the entire q (where $q = 4\pi\sin\theta/\lambda$, θ and λ being half of the scattering angle and the wavelength, respectively) range examined (0.5–40 nm^{-1}) are represented in Figure S2. For comparison, the XRD pattern of the nondoped host matrix m-A(14) has also been included.[15] In the high q range ($q > 12$ nm^{-1}) the most intense event observed in all the diffractograms (Figure S2) is a broad band centred at $q = 15$ nm^{-1}, associated with ordering within the siliceous domains,[27] amide–amide spacing[10c] and chain–chain spacing.[28] Characteristic distances, d = 0.42–0.41 nm, were calculated by using the Bragg law. The coherence length, L, over which the structural unit survives was estimated by using the modified Sherrer equation $L = I\lambda/(A\cos\theta)$ (where A, in radians, is the integrated area of the peaks and I is the corresponding maximum intensity). A value of $L \approx 8.6$ nm was deduced.

The reflections discerned in the low q range ($q < 12$ nm^{-1}) of the XRD patterns of the Eu^{3+}-doped m-A(14) mono-amidosils with n = 200, 60 and 10 reproduced in Figure 1 are ascribed to the kth order peaks of two lamellar structures with different spacing l (where $l = k2\pi/q_k$). Curve-fitting by means of Voight shapes allowed us to resolve the first peak detected in the XRD patterns of the doped compounds into two components. The position of one of these components coincides exactly with that of the first peak of the XRD pattern of the m-A(14) matrix, a result that strongly supports the fact that, in the Eu(CF$_3$SO$_3$)$_3$-doped m-A(14)-based mono-amidosils, the lamellar structure of the m-A(14) host hybrid framework ($l = 5.0 \pm 0.2$ nm[15]) coexists with a new one (also lamellar bilayer) exhibiting lower spacing. Remarkably, neither at n = 200 nor at n = 60 is the growth of this second lamellar phase accompanied by the formation of crystallites of pure salt. In fact, only in the case of the most concentrated m-A(14)-based mono-amidosil studied (n = 10) is the presence of free Eu(CF$_3$SO$_3$)$_3$ detected (see asterisks in the corresponding XRD pattern in Figure 1). These data suggest that, at n = 200 and 60, the Eu^{3+} ions added to m-A(14) bond to the only available coordinating groups provided by this host hybrid matrix, that is, the C=O oxygen atoms of the amide cross-links, meaning that in both samples the salt is practically dissociated by the host framework. Hence the most extraordinary structural effect arising from salt ad-

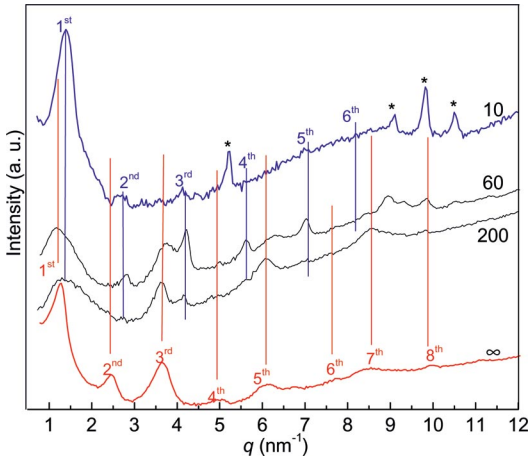

Figure 1. XRD patterns of the m-A(14)$_n$Eu(CF$_3$SO$_3$)$_3$ mono-amidosils. Diffracting peaks produced by the pure salt are indicated by asterisks.

dition is the formation of a lamellar ordered phase, which is itself composed of Eu^{3+} ions. Also noteworthy is the fact that the emergence of this new Eu^{3+}-containing highly ordered phase is not accompanied by the destruction of the original lamellar structure of m-A(14), which remains completely unaffected. The expected dramatic consequences of the whole process on the extent and strength of hydrogen bonding and on ionic association will be discussed in depth below. At high salt content (n = 10), the m-A(14)-based lamellar structures [the original m-A(14) and the new Eu^{3+}-based one] are no longer able to accommodate all the salt incorporated, and, as a consequence, a part of it will be expelled. In spite of this "salting-out" effect, in the sections that follow, this sample will be used for comparison purposes, because of its inherent lamellar structure.

In contrast with the lamellar structural organization detected in the $Eu(CF_3SO_3)_3$-doped m-A(14)-based mono-amidosils investigated here, XRD studies revealed that the shorter-chain m-A(8)$_n$Eu$(CF_3SO_3)_3$ samples (results not shown) are entirely amorphous.

The DSC curves of the m-A(14)$_n$Eu$(CF_3SO_3)_3$ hybrids with n = 200 and 60 in the 20–150 °C range are represented in Figure 2. The analysis of the thermal behaviour of the doped samples is fundamental. In m-A(14), self-assembly is governed by intermolecular hydrogen bonding between amide groups, tail-to-tail van der Waals interactions between *all-trans* methyl-terminated alkyl chains assuming a partially interdigitated packing mode and an entropic term related to the phase separation between the alkyl chains and the siloxane nanodomains.[15] The self-assembly forces determine the emergence of a thermally actuated photoluminescence memory effect induced by a reversible order–disorder phase transition of the alkyl chains (T_{onset} = 96 °C and T_{peak} = 106 °C, ΔH = 30.44 J g^{-1} and ΔS = 0.287 J g^{-1} C^{-1}) achieved by heating/cooling cycles between room temperature and 120 °C, which, in turn, lead to a hysteretic behaviour of the emission energy.[15]

Figure 2 demonstrates that the addition of $Eu(CF_3SO_3)_3$ to m-A(14) has marked consequences and supports the coexistence of two crystalline phases in the doped m-A(14)-based mono-amidosils. The sample with n = 200 gives rise to a strong endotherm centred at 117 °C (T_{onset} ≈ 100 °C, ΔH = 42.40 J g^{-1} and ΔS = 0.362 J g^{-1} C^{-1}) and a very weak, ill-defined peak, also endothermic, located at about 97 °C. A broad endotherm centred at 99 °C, displaying a shoulder at approximately 94 °C (T_{onset} ≈ 82 °C), dominates the DSC curve of m-A(14)$_{60}$Eu$(CF_3SO_3)_3$. In addition, in the thermograms of both doped mono-amidosils, a third peak is also detected at about 73 °C (Figure 2).

The endotherms produced by the samples with n = 200 and 60 at 117 and 99 °C, respectively, may be unequivocally attributed to the order–disorder phase transition of the nondoped lamellar structure of the m-A(14) host hybrid framework. The peak temperature upshift and the simultaneous increase in the enthalpy and entropy values occurring in the most dilute mono-amidosil with respect to the values reported for the nondoped matrix prove that the energetics of the melting process of the pendant alkyl chains of m-

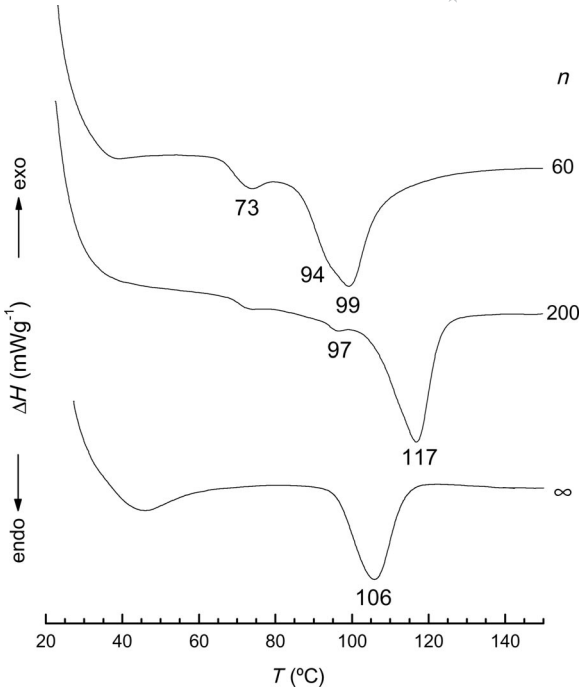

Figure 2. DSC curves of the m-A(14)$_n$Eu$(CF_3SO_3)_3$ mono-amidosils.

A(14) are, as expected, deeply altered upon incorporation of the guest salt. Nagle and Goldstein[29] showed that, during the melting transition of alkyl chains, most of the enthalpy change is accounted for by a large cohesive van der Waals energy term and the entropy change is accounted for by a conformational term, an excluded volume term and a dominating volume expansion term. The peak found at 97 °C (very weak) and 94 °C (strong) in samples with n = 200 and 60, respectively, is associated with the order–disorder transition of the new lamellar phase formed in the presence of $Eu(CF_3SO_3)_3$, as suggested by XRD. This result clearly demonstrates that salt doping is a useful tool to lower the phase transition temperature of the original lamellar phase of m-A(14). Systematic studies that are being carried out at present with mono- and divalent triflate salts confirm this claim. Lowering the order–disorder phase transition temperature is of paramount importance, as it will allow increasing the number of heating/cooling cycles without causing significant structural changes in the material. The origin of the peak at 73 °C will remain unknown.

The TGA curve of the dilute m-A(14)$_{200}$Eu$(CF_3SO_3)_3$ exhibits a single weight loss with onset at about 325 °C [Figure S3(a)]. This finding proves that in a non-oxidizing atmosphere the addition of $Eu(CF_3SO_3)_3$ to m-A(14) exerts a stabilizing thermal effect on this host hybrid network for which the beginning of decomposition was detected at around 300 °C.[15]

In the TGA curve of m-A(8)$_{40}$Eu$(CF_3SO_3)_3$ [Figure S3(b)], a single weight loss with onset at about 340 °C is observed. The TGA curve of the m-A(8)$_{10}$Eu$(CF_3SO_3)_3$ mono-amidosil reveals that its decomposition is initiated with a slight weight loss beyond 210 °C, followed by a dra-

matic weight loss around 330 °C [Figure S3(b)]. This leads us to conclude that at both concentrations (i.e., n = 40 and 10) $Eu(CF_3SO_3)_3$ destabilizes the m-A(8) system that starts to suffer thermal degradation at approximately 400 °C.[20]

2.3. Chain Packing and Conformational Disorder

To gain insight into the structural and phase-state of the alkyl chains of the mono-amidosils synthesized, we examined two diagnostic modes of the hydrocarbon chains in the FTIR spectra: the symmetric and asymmetric CH_2 modes (ν_sCH_2 and ν_aCH_2, respectively). The frequency, width and height of these modes are sensitive to the *gauche*/*trans* conformational ratio and to the intermolecular interactions occurring between the alkyl chains.[11,30] Typically the ν_sCH_2 and ν_aCH_2 bands of crystalline alkyl chains (*all-trans* conformations) are located at lower wavenumbers than those of amorphous alkyl chains (*gauche* conformations) (Table S2). The FTIR spectra of the m-A(14)$_n$Eu$(CF_3SO_3)_3$ and m-A(8)$_n$Eu$(CF_3SO_3)_3$ compounds in the ν_aCH_2 and ν_sCH_2 regions are shown in Figures 3(a) and 3(b), respectively. Their frequency and full-width-at-half-maximum (fwhm) are gathered in Table 2.

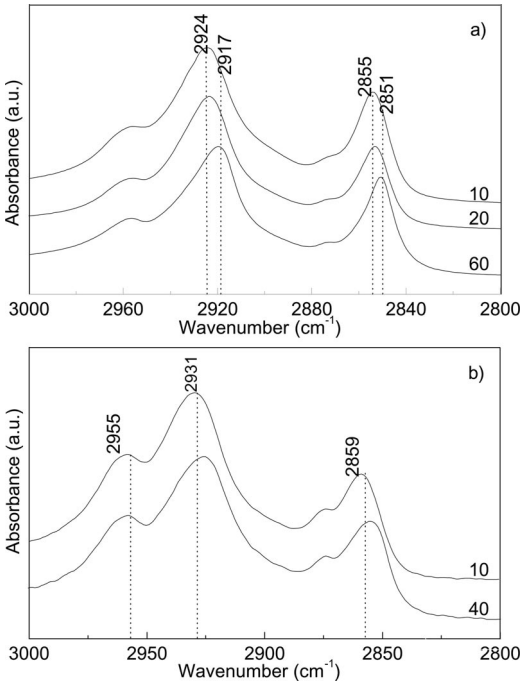

Figure 3. FTIR spectra of the m-A(14)$_n$Eu$(CF_3SO_3)_3$ (a) and m-A(8)$_n$Eu$(CF_3SO_3)_3$ (b) mono-amidosils in the ν_aCH_2 and ν_sCH_2 regions.

Analysis of Figure 3(a) and Table 2 demonstrates that the signature of the m-A(14)$_{60}$Eu$(CF_3SO_3)_3$ mono-amidosil resembles closely that of m-A(14)[15] in the ν_aCH_2 and ν_sCH_2 regions, a proof that in this Eu^{3+}-containing sample the population of alkyl chains that adopt *all-trans* conformations is largely dominant. This means that at n = 60 the great majority of chains of m-A(14) are fully stretched, densely packed and highly ordered. Considering that at this salt concentration the characteristic lamellar phase of m-A(14) is formed concomitantly with a new one, also of lamellar type, this result is indeed quite exceptional, as it supports the explanation that, in spite of the coordination of Eu^{3+} ions to the C=O groups of the amide cross-links and of the steric hindrance that is expected to result in parallel, the degree of order of the alkyl chains remains unaffected. At $n \leq 20$, the intensity maximum of both bands shifts to higher wavenumbers and the fwhm increases, too [Figure 3(a) and Table 2]. This spectral evidence proves that, over this range of concentrations, salt addition induces chain disorder, meaning that the population of alkyl chains in *gauche* conformations increases significantly and becomes dominant.[11,30]

Table 2. Characteristics bands of the FTIR spectra of the m-A(14)$_n$Eu$(CF_3SO_3)_3$ and m-A(8)$_n$Eu$(CF_3SO_3)_3$ mono-amidosils in the $\nu_a(CH_2)$ and $\nu_s(CH_2)$ regions.

x	n	$\nu_a(CH_2)$ ν (cm^{-1})	fwhm	$\nu_s(CH_2)$ ν (cm^{-1})	fwhm
14	∞[15]	2919	21	2850	10
	60	2920	24	2854	15
	20	2924	26	2855	15
	10	2924	27	2856	15
8	∞[20]	2929	34	2856	10
	40	2929	33	2858	12
	10	2930	34	2859	10

The spectroscopic data in Figure 3(b) and Table 2 confirm that the incorporation of Eu^{3+} ions into the m-A(8) matrix does not affect the degree of disorder of the alkyl chains, which continue to adopt *gauche* conformations,[11,30] a finding that corroborates the XRD conclusions.

2.4. Cation/Amide Cross-Link Interactions and Hydrogen Bonding

Seeking the elucidation of the strength and extent of hydrogen bonding in the Eu^{3+}-containing m-A(14)- and m-A(8)-based mono-amidosils, we investigated the Amide I and Amide II regions of the FTIR spectra. Another goal of this spectroscopic analysis was to determine the ranges of salt concentration in which the C=O oxygen atoms of the amide cross-links bond to the Eu^{3+} ions.

Several scenarios may be envisaged for the lanthanide ions upon doping: they may bond either to the oxygen atoms of the C=O groups of the amide cross-links of the host m-A(x) mono-amidosil matrix or to the oxygen atoms of the $CF_3SO_3^-$ ions or even to both. In terms of Eu^{3+} coordination to the C=O groups, two situations are possible: (1) direct bonding to "free" (non-hydrogen-bonded) C=O groups; (2) interaction with C=O groups made free through the destruction of hydrogen-bonded amide–amide aggregates of the host framework.

The Amide I region (1800–1600 cm^{-1}),[31] essentially a C=O stretching mode, is sensitive to the specificity and magnitude of hydrogen bonding. Therefore the Amide I envelope usually consists of several individual components corresponding to different environments of the C=O

groups.[32] For instance, the Amide I region of amorphous polyamides displays an intense band at 1640 cm^{-1} and a shoulder at about 1671 cm^{-1}, attributed to hydrogen-bonded and "free" C=O groups, respectively.[32] The Amide II region (1600–1500 cm^{-1}), mainly associated with the N–H in-plane bending vibration ($\delta_{i.p.}$NH), is sensitive to chain conformation and intermolecular hydrogen bonding, providing information about the distribution of hydrogen bond strengths. When the amide group is included in hydrogen-bonded aggregates, the characteristic $\delta_{i.p.}$NH band of "free" amide is upshifted. In the case of amorphous polyamides, the Amide II band emerges at 1545 cm^{-1}.[32]

The FTIR spectra of the m-A(14)$_n$Eu(CF$_3$SO$_3$)$_3$ and m-A(8)$_n$Eu(CF$_3$SO$_3$)$_3$ mono-amidosils in the Amide I and Amide II regions are reproduced in Figures S4(a) and S4(b), respectively. The results of the curve-fitting performed in the 1750–1450 cm^{-1} interval are illustrated in Figures 4(a) and 4(b), respectively. The frequency, integral area and assignment of the individual Amide I and Amide II components are given in Table 3. The variation of the integral area of the resolved Amide I components with n is depicted in Figures S5(a) and S5(b), respectively.

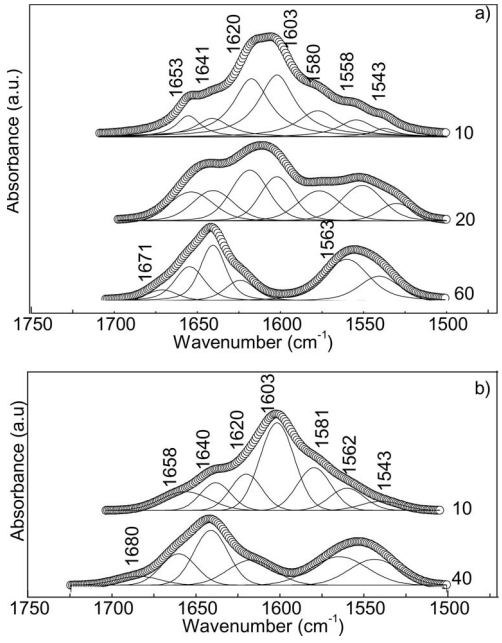

Figure 4. Curve-fitting results of the Amide I and Amide II bands of the m-A(14)$_n$Eu(CF$_3$SO$_3$)$_3$ (a) and m-A(8)$_n$Eu(CF$_3$SO$_3$)$_3$ (b) mono-amidosils.

The Amide I and Amide II band profiles of the m-A(14)$_n$-Eu(CF$_3$SO$_3$)$_3$/m-A(8)$_n$Eu(CF$_3$SO$_3$)$_3$ mono-amidosils with n = 60/40 and 10/10 are very similar [Figure S4(a)/Figure S4(b)]. Interestingly, the frequency difference between the Amide I and Amide II intensity maxima in the mono-amidosils m-A(14)$_{60}$Eu(CF$_3$SO$_3$)$_3$ and m-A(8)$_{40}$Eu-(CF$_3$SO$_3$)$_3$ ($\Delta\nu$ = 87 cm^{-1}) coincides with that reported for m-A(14),[15] an indication that the hydrogen-bonded array in the three samples is considerably stronger than that formed in m-A(8) ($\Delta\nu$ = 97 cm^{-1}).[20] Also noteworthy is the emergence of a new, very intense band centred at approximately 1604 cm^{-1} in the spectra of m-A(14)$_{20}$Eu(CF$_3$SO$_3$)$_3$ and m-A(8)$_{10}$Eu(CF$_3$SO$_3$)$_3$ [Figures S4(a) and S4(b), respectively]. Figures S5(a) and S5(b) provide a very clear view of the set of tremendous modifications undergone by the characteristic hydrogen-bonded amide–amide aggregates of m-A(14) and m-A(8) upon incorporation of the Eu^{3+} ions over the whole range of salt concentrations examined.

Table 3. Components of the FTIR Amide I and Amide II bands (cm^{-1}) of the m-A(14)$_n$Eu(CF$_3$SO$_3$)$_3$ and m-A(8)$_n$Eu(CF$_3$SO$_3$)$_3$ mono-amidosils.

m-A(14)$_n$Eu(CF$_3$SO$_3$)$_2$				
∞[15] ν (fwhm)	60 ν (fwhm)	20 ν (fwhm)	10 ν (fwhm)	Type
	1671 (21)	–	–	F
1652 (27)	1652 (21)	1653 (31)	1653 (18)	D
1640 (17)	1640 (18)	1641 (28)	1639 (25)	O1
1625 (15)	1623 (21)	1619 (26)	1617 (26)	O2
–	–	1603 (23)	1604 (27)	O3
	–	1578 (29)	1581 (29)	O3
1560 (24)	1562 (32)	1557 (28)	1560 (26)	
1545 (25)	1543 (28)	1543 (23)	1542 (18)	
m-A(8)$_n$Eu(CF$_3$SO$_3$)$_2$				
∞[20] ν (fwhm)	40 ν (fwhm)		10 ν (fwhm)	Type
1676 (34)	1680 (31)		–	F
1657 (24)	1660 (24)		1658 (33)	D
1643 (20)	1640 (24)		1639 (21)	O1
1626 (20)	1618 (33)		1621 (22)	O2
–	–		1603 (24)	O3
–	–		1581 (23)	O3
1561 (38)	1564 (39)		1561 (24)	
1546 (31)	1543 (35)		1541 (28)	

The band at 1671/1680 cm^{-1} observed in the FTIR spectra of the two series of Eu^{3+}-doped mono-amidosils is ascribed to "free" C=O groups (F).[32b,15] The absence of this feature at n = 20/10 means that, at these salt contents, the C=O groups of the amide cross-links become saturated. The band produced at about 1653/1660 cm^{-1} by all the m-A(x)$_n$Eu(CF$_3$SO$_3$)$_3$ mono-amidosils analyzed is attributed to hydrogen-bonded C=O groups in disordered amide–amide aggregates (D).[32b,15] The events situated near 1640 and 1620 cm^{-1} are assigned to hydrogen-bonded C=O groups in ordered amide–amide aggregates (O1 and O2, respectively) of increasing strength.[32b,15] The new Amide I (1602 cm^{-1}) and Amide II (1581 cm^{-1}) components detected in the FTIR spectra of both families of mono-amidosils at $n \leq$ 20/10 may be correlated with the formation of very strong and ordered Eu^{3+}-coordinated amide–amide aggregates (O3). Figure S5(a) shows that the latter aggregates are formed at the expense of the destruction of aggregates D and O1 in the case of the m-A(14)$_n$Eu(CF$_3$SO$_3$)$_3$ series. The effect is, however, considerably more dramatic in the m-A(8)$_n$Eu(CF$_3$SO$_3$)$_3$ mono-amidosil family, in which the significant amount of aggregates O3 formed implies the partial breakdown of the D, O1 and O2 aggregates and the complete saturation of the "free" C=O groups [Figure S5(b)].

An interesting effect worth mentioning is the presence of the band ascribed to "free" C=O groups in the spectrum of m-A(14)$_{60}$Eu(CF_3SO_3)$_3$, in spite of the fact that this event is not produced by m-A(14) [Figure S5(a)]. The reason for the existence of a minor population of "free" C=O groups at n = 60 is very likely a manifestation of the formation of the new lamellar phase, which is accompanied by a major breakdown of aggregates D and O1 and an increase in the fraction of aggregates O2.

Not surprisingly, this spectral analysis has demonstrated that globally the addition of Eu(CF_3SO_3)$_3$ to m-A(14) and m-A(8) has similar consequences on the hydrogen-bonded array of both host matrices.

2.5. Cation/Anion Interactions

To determine the nature of the anionic configurations formed in the two series of mono-amidosils investigated here, we analyzed the non-degenerate symmetric stretching vibration ($\upsilon_s SO_3$) mode of the triflate ion in the FTIR spectra of the materials. When the anion is "free", this mode is located at 1032 cm^{-1}.[33] Shifts of the $\upsilon_s SO_3$ band to lower and higher wavenumbers result upon coordination to a cation.[34–36]

The FTIR spectra of the m-A(14)$_n$Eu(CF_3SO_3)$_3$ and m-A(8)$_n$Eu(CF_3SO_3)$_3$ mono-amidosils in the $\upsilon_s SO_3$ region are represented in Figures S6(a) and S6(b), respectively. The results of the curve-fitting performed in the 1070–1010 cm^{-1} interval are reproduced in Figures 5(a) and 5(b), respectively.

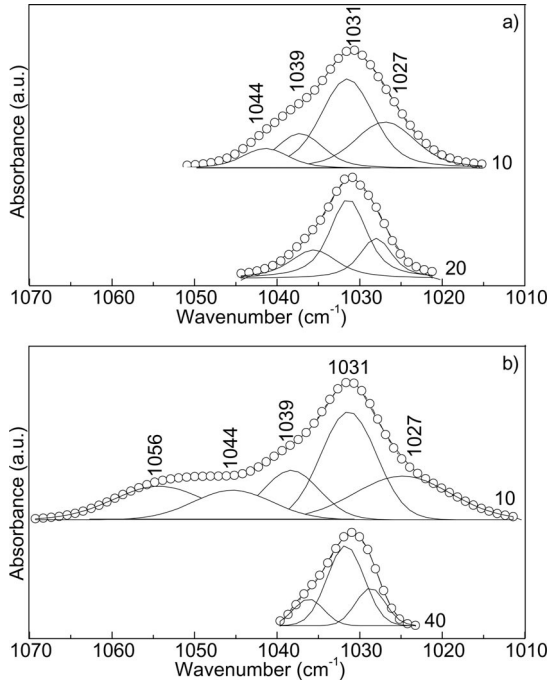

Figure 5. Curve-fitting results of the $\upsilon_s SO_3$ region of the FTIR spectra of the m-A(14)$_n$Eu(CF_3SO_3)$_3$ (a) and m-A(8)$_n$Eu(CF_3SO_3)$_3$ (b) mono-amidosils.

The occurrence of the 1031 cm^{-1} band in the FTIR spectra of the doped mono-amidosils with $n \geq 10$ confirms the occurrence of "free" anions over the whole range of salt concentrations examined.[33] This band also very probably receives the contribution of the "cross-link-separated ion pairs".[37] The shoulders observed at approximately 1027 and 1039 cm^{-1} in all the samples are associated with weakly coordinated triflate ions located in two different types of sites:[36] (1) $CF_3SO_3^-$ species weakly bonded to the Eu^{3+} ions, which simultaneously interact with the C=O oxygen atoms of the amide groups; (ii) $CF_3SO_3^-$ ions hydrogen-bonded to the amide N–H groups. The 1044 cm^{-1} event detected at n = 10 in both families of mono-amidosils and that observed at 1056 cm^{-1} in the case of the m-A(8)$_{10}$Eu(CF_3SO_3)$_3$ sample are associated with ionic aggregates of increasing complexity and unknown composition and charge. Thus, ionic association appears to be more favoured in the m-A(8)-based mono-amidosils than in the m-A(14)-based ones.

2.6. Photoluminescence

Figure 6(a) shows the room-temperature emission spectra of selected Eu^{3+}-doped m-A(x) hybrids under different excitation wavelengths. All spectra consist of a large broad band, superimposed on a series of straight lines ascribed to the $^5D_0 \rightarrow {}^7F_{0-4}$ Eu^{3+} intra-4f^6 transitions. The broad band has already been observed in the nondoped m-A(8)[20] and m-A(14)[15] mono-amidosils and in similar organic–inorganic hybrids[38] and may be ascribed to electron–hole recombinations occurring within oxygen-related defects present in the siliceous domains and within the amide cross linkages.[38] While the energy of the broad band is almost independent of the number of CH_2 groups and Eu^{3+} concentration, their relative intensity with respect to the intra-4f^6 lines decreases as the amount of Eu^{3+} increases. This observation is in good agreement with the existence of hybrid host-to-Eu^{3+} energy transfer.[39,40] The energy, fwhm and relative intensity of the intra-4f^6 lines strongly depend on the excitation wavelength, pointing out the presence of distinct Eu^{3+} local environments in each hybrid, as discussed in detail below.

The excitation spectra were monitored between 14 and 300 K along the backbone emission of the hybrid and within the $^5D_0 \rightarrow {}^7F_2$ transition. The spectra display a large broad band (300–450 nm), which is redshifted and enlarged as the monitoring wavelength increases, as exemplified in Figure 6(b) for m-A(14)$_{10}$Eu(CF_3SO_3)$_3$. These excitation spectra features resemble those of the nondoped diureasils,[16,40] so that the high- and low-wavelength region of the spectra can be assigned to the preferential excitation of the siliceous and amide cross linkages. The excitation spectra monitored within the $^5D_0 \rightarrow {}^7F_2$ transition are mainly composed of a broad band centred at 350 nm and 325 nm for m-A(8)$_{40}$Eu(CF_3SO_3)$_3$ and m-A(14)$_{60}$Eu(CF_3SO_3)$_3$, respectively, overlapping with a series of sharp lines assigned to transitions between the $^7F_{0,1}$ levels of the ground multiplet

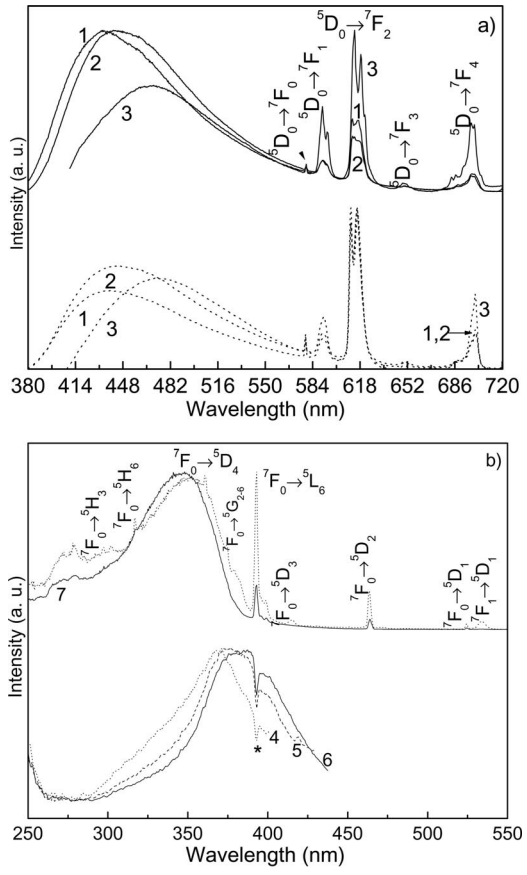

Figure 6. Room-temperature (a) emission spectra excited at (1) 340 nm, (2) 361 nm and (3) 393 nm and (b) excitation spectra monitored at (4) 445 nm, (5) 470 nm, (6) 490 nm and (7) 612 nm of (solid line) the m-A(8)$_{40}$Eu(CF$_3$SO$_3$)$_3$ and (dotted line) m-A(14)$_{60}$-Eu(CF$_3$SO$_3$)$_3$ mono-amidosils. The asterisk denotes the $^7F_0 \rightarrow {}^5L_6$ self-absorption.

and the excited states. The broad band is ascribed to a ligand-to-metal charge transfer (LMCT) transition resulting from the interaction of the Eu^{3+} ion and the first ligands.[40,41] The m-A(14)$_n$Eu(CF$_3$SO$_3$)$_3$ mono-amidosils present a LMCT band at higher energy than those displayed by the m-A(8)$_n$Eu(CF$_3$SO$_3$)$_3$ hybrids, within the whole concentration range studied here. The shift of the LMCT band towards the high-energy region of the spectrum can be ascribed to an increase in the effective charge of the lanthanide cation and to a decrease in the covalency of the Eu^{3+}–first-ligand bonds.[41] Therefore, we may infer more covalent Eu^{3+}–ligand bonds in m-A(8)$_n$Eu(CF$_3$SO$_3$)$_3$ hybrids than in the case of the m-A(14)$_n$Eu(CF$_3$SO$_3$)$_3$ mono-amidosils, because of alterations in the type and/or number of ligands present in the first coordination shell.

The relative intensity of the LMCT band, with respect to that of Eu^{3+} lines, increases drastically when the temperature is decreased to 14 K (Figure S7), suggesting a thermally deactivated mechanism, in accordance with the non-radiative mechanism typically associated with the presence of LMCT states.[42] Apart from changes in the relative intensity between the LMCT states and the intra-4f^6 lines, no major changes are observed in the excitation spectra as the concentration decreases from n = 10 to n = 200 in both hybrid families, indicating that the same excitation paths are present.

The energy, fwhm and relative intensity of the intra-4f^6 lines strongly depend on the excitation wavelength. The most notorious changes are related with variations in the relative intensity of the $^5D_0\rightarrow{}^7F_{0\text{–}4}$ transitions, changing from direct intra-4f^6 excitation to excitation through the LMCT sates. In particular, under direct intra-4f^6 excitation into the $^5L_6$ level (393 nm) and $^5D_2$ level (465 nm), an increase in the relative intensity of the $^5D_0\rightarrow{}^7F_{1,4}$ transitions is observed, whereas no significant changes are detected for the remaining transitions, relative to those in the spectrum excited at 350 nm (Figure S8). This observation is independent of the Eu^{3+} concentration and number of CH_2 groups, as illustrated for selected hybrids in Figures S8 and S9. These two Eu^{3+} local sites will afterwards be identified as sites A (favoured by intra-4f^6 direct excitation) and B (selectively excited through LMCT sates). The presence of a similar site A (characterized by a low-symmetry local coordination with an inversion centre and without the $^5D_0\rightarrow{}^7F_0$ transition) was already reported for diurethane cross-linked hybrids and attributed to weakly coordinated Eu^{3+}/$CF_3SO_3^-$ ion pairs.[43] The presence of site A in the m-A-(x)$_n$Eu(CF$_3$SO$_3$)$_3$ mono-amidosils is in good agreement with the FTIR spectroscopic results discussed above, which demonstrate that the $CF_3SO_3^-$ anions exist "free", weakly coordinated and presumably form cross-link separated ion pairs.

We will now focus our attention on the analysis of site B, as it is selectively excited through the LMCT states, therefore involving an active contribution from the hybrid host in the Eu^{3+} coordination through the oxygen atoms of the C=O groups, as suggested by results of XRD analysis and FTIR spectroscopy. Moreover, owing to the fact that site B is selectively excited through the LMCT states, the discussion can be conducted independently of the presence of site A.

Figure 7(a) shows the $^5D_0\rightarrow{}^7F_{0\text{–}4}$ transitions scanned at 14 K with high resolution as function of the Eu^{3+} concentration for m-A(14)- and m-A(8)-based hybrids. In the former hybrids and for $20<n\leq200$, the intra-4f^6 energy and fwhm are almost independent of the Eu^{3+} concentration, whereas at high Eu^{3+} concentrations ($10\leq n\leq20$), major changes in the energy are discerned. This observation points out changes in the Eu^{3+} local environment. To monitor these variations, the energy and fwhm of the $^5D_0\rightarrow{}^7F_0$ transition was calculated by using a single Gaussian function fit [Figure 7(b)].

Independently of the concentration, a single line with approximately the same fwhm value (33.0 ± 1.0 cm^{-1}) was estimated, indicating the presence of a single average local environment in each hybrid. However, the energy of the $^5D_0\rightarrow{}^7F_0$ transition is approximately the same for $60\leq n\leq200$, 17247.3 ± 0.2 cm^{-1} and 17251.6 ± 0.2 cm^{-1} for n = 200 and n = 60, respectively. Upon increasing the concentration, the $^5D_0\rightarrow{}^7F_0$ energy deviates towards the blue becoming 17263.5 ± 0.5 cm^{-1} for n = 20 and n = 10. These

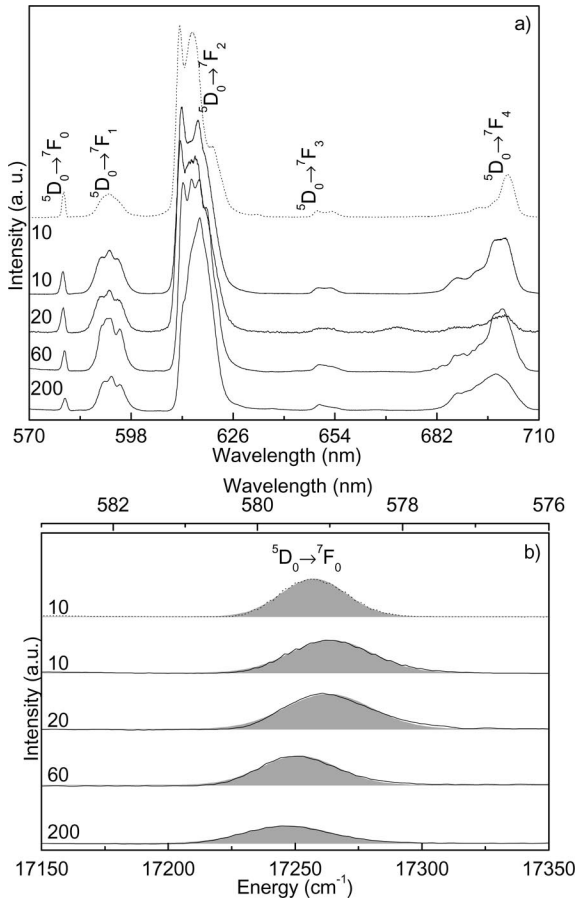

Figure 7. (a) Emission spectra (14 K) of (solid line) the m-A(14)$_n$-Eu(CF$_3$SO$_3$)$_3$ and (dotted line) m-A(8)$_n$Eu(CF$_3$SO$_3$)$_3$ mono-amidosils, excited within the LMCT states (335–350 nm). (b) Magnification of the $^5D_0\rightarrow{}^7F_0$ transition. The shadow represents the best fit obtained by using a single Gaussian function.

energy interval values and the energy blueshift observed upon increasing the amount of Eu^{3+} resemble those reported for diurethane cross-linked hybrids.[43]

The energy of the $^5D_0\rightarrow{}^7F_0$ transition is usually correlated with the so-called nephelauxetic effect induced by the ion first neighbours in such a way that a blueshift of the $^5D_0\rightarrow{}^7F_0$ transition is correlated with Eu^{3+} local sites in which the metal–ligand bonds have a lower covalency degree.[44] Therefore, we may interpret the blueshift of the $^5D_0\rightarrow{}^7F_0$ energy upon increasing the amount of Eu^{3+} in terms of variations in the number or type of first neighbours.

The effect of the decrease in the number of CH_2 groups from 14 to 8 was studied by comparing the energy and fwhm of the $^5D_0\rightarrow{}^7F_0$ transition for n = 10 [Figure 6(b)]. The energy and fwhm of such a transition for m-A(8)$_{10}$-Eu(CF$_3$SO$_3$)$_3$ are 17257.3 ± 0.1 cm^{-1} and 25.6 ± 0.2 cm^{-1}, respectively. This energy value is slightly redshifted relative to that found for m-A(14)$_{10}$Eu(CF$_3$SO$_3$)$_3$ (17263.5 ± 0.5 cm^{-1}), suggesting that the Eu^{3+}–first-ligand bonds exhibit a higher degree of covalency in the mono-amidosils with shorter pendant alkyl chains, in accordance with the results aforementioned for the energy of the LMCT band. Furthermore, the lower fwhm value found for the amorphous m-A(8) host points out that the lamellar nature of the m-A(14) hybrids imposes a larger distribution of closely similar Eu^{3+} local coordination sites, relative to that found in the amorphous m-A(8) hybrids.

For all the hybrids, the $^5D_0$ emission decay curves were monitored within the $^5D_0\rightarrow{}^7F_{0,2}$ transitions under excitation through the LMCT states, in order to selectively excite site B. All the curves revealed a single exponential behaviour, yielding the lifetime values gathered in Table 4. The lifetime values are very similar for all the hybrids, in good agreement with a similar Eu^{3+} local environment, independently of the Eu^{3+} concentration and number of CH_2 groups of the alkyl chain.

Table 4. $^5D_0$ lifetime values (τ) obtained under LMCT excitation (λ_{ex}), absolute emission quantum yield (ϕ), number of water molecules coordinated to each Eu^{3+} ion ($n_w \pm 0.1$), $^5D_0$ quantum efficiency (η), radiative transition probability (A_r) and nonradiative transition probability (A_{nr}) for the m-A(x)$_n$Eu(CF$_3$SO$_3$)$_3$ hybrids.

	n	λ_{ex} (nm)	τ (ms)	ϕ	n_w	η	A_r (ms^{-1})	A_{nr} (ms^{-1})
m-A(8)$_n$Eu-(CF$_3$SO$_3$)$_3$	10	345	0.365±0.006	0.06	1.9	0.25	0.685	2.055
	40	350	0.386±0.006	0.08	1.8	0.23	0.596	1.995
m-A(14)$_n$Eu-(CF$_3$SO$_3$)$_3$	10	321	0.349±0.005	0.03	2.3	0.15	0.430	2.436
	60	340	0.447±0.007	0.07	1.6	0.19	0.425	1.812
	200	350	0.360±0.007	0.08	2.2	0.17	0.472	2.306

The $^5D_0$ radiative (A_r) and nonradiative (A_{nr}) transition probabilities and the $^5D_0$ quantum efficiency (η) [$\eta = A_r/(A_r+A_{nr})$] can be estimated on the basis of the emission spectrum and the $^5D_0$ lifetime ($\tau^{-1} = A_r + A_{nr}$).[16] The radiative contribution in the case of Eu^{3+}-based materials may be calculated from the relative intensities of the $^5D_0\rightarrow{}^7F_{0-4}$ transitions (the $^5D_0\rightarrow{}^7F_{5,6}$ branching ratios are neglected due to their small relative intensity with respect to that of the remaining $^5D_0\rightarrow{}^7F_{0-4}$ lines). The $^5D_0\rightarrow{}^7F_1$ transition does not depend on the local ligand field and may therefore be used as a reference for the whole spectrum. An effective refractive index of 1.5 was used, leading to $A_{01} \approx 50$ s^{-1} (A_{01} stands for Einstein's coefficient of spontaneous emission between the $^5D_0$ and the $^7F_1$ Stark levels). Furthermore, the absolute emission quantum yield (ϕ) was also measured. This experimentally evaluated quantity is given by the ratio of the number of emitted photons to the number of absorbed ones and includes absorption efficiency, intersystem crossing efficiency, host–Eu^{3+} energy transfer efficiency, the efficiency of intra-Eu^{3+} nonradiative decay paths and the $^5D_0$ quantum efficiency (η).[16] Therefore: $\phi \leq \eta$.

The η values found for the m-A(8)$_n$Eu(CF$_3$SO$_3$)$_3$ hybrids are slightly higher than those calculated for m-A(14)$_n$Eu-(CF$_3$SO$_3$)$_3$ mono-amidosils, essentially because of a higher A_r value. These η values are similar to those reported for other Eu^{3+}-doped lamellar-bridged silsesquioxanes.[19] Generally, high η values are only found in the case of LMCT positions above 40000 cm^{-1}.[45] As the LMCT states we are

looking at are positioned at considerably lower energies (27000–29000 cm^{-1}), an important overlap with the ion levels clearly contributes to the effective depopulation of the $^5D_0$ level in the mono-amidosils. The variations in η and A_{nr} values may be rationalized in terms of the number of water molecules coordinated to the Eu^{3+} ions (n_w) on the basis of: $n_w = 1.1 \times (\tau^{-1} - A_r - 0.31)$.[46] An average number of two water molecules was estimated for all the hybrids.

3. Conclusion

In the present work, we have investigated Eu^{3+}-doped mono-amide cross-linked alkyl/siloxane hybrids, designated as *mono-amidosils*, in which short methyl-capped alkyl chains are grafted to the siliceous framework through amide groups. The thermal analysis data allowed us to conclude that, in the more dilute m-A(14)$Eu(CF_3SO_3)_3$ materials, the salt exerts a stabilizing effect on the m-A(14) matrix. However, the addition of $Eu(CF_3SO_3)_3$ destabilizes the m-A(8) system. The m-A(8)$_n$$Eu(CF_3SO_3)_3$ mono-amidosils are all amorphous, whereas the m-A(14)-based mono-amidosils exhibit a lamellar structure. Doping the m-A(14) matrix with Eu^{3+} ions induces the formation of a new and highly organized lamellar structure, which coexists with the characteristic lamellar structure of the m-A(14) matrix. In the dilute Eu^{3+}-doped m-A(14) mono-amidosils ($n > 20$), the alkyl chains adopt *all-trans* conformations. However, the increase in salt content ($n \leq 20$) leads to a marked increase in the population of *gauche* conformers. In the case of the m-A(8)$_n$$Eu(CF_3SO_3)_3$ mono-amidosil family, the alkyl chains adopt *gauche* conformations in all the salt concentrations analyzed. The hydrogen-bonded associations formed at high salt content in the Eu^{3+}-doped mono-amidosils are more ordered (and consequently stronger) than those found in the less concentrated hybrids and in the m-A(14) and m-A(8) matrix. The mono-amidosils are white light emitters (maximum quantum yield 0.08 ± 0.01), presenting an broad emission band in the blue/purplish-blue spectral region ascribed to electron–hole recombinations (occurring within oxygen-related defects present in the siliceous domains and within the amide cross linkages) superimposed on the $^5D_0 \rightarrow {}^7F_{0-4}$ Eu^{3+} intra-4f^6 transitions. Two Eu^{3+} local coordination sites (named A and B) were discerned over the whole concentration range. Site A is attributed to weakly coordinated $Eu^{3+}/CF_3SO_3^-$ ion pairs, whereas site B involves coordination to the oxygen atoms of the C=O groups, of the $CF_3SO_3^-$ ions and of the water molecules (ca. 2). For the m-A(8) amorphous hybrid host, the Eu^{3+}–first-ligand bonds in site B present a higher degree of covalency. We may speculate that this higher degree of covalency is due to the coordination to a higher number of C=O oxygen atoms, relative to m-A(14). In spite of the natural higher tendency of C=O oxygen atoms to bond covalently to the Eu^{3+} ions than those of the oxygen atoms of water molecules and SO_3 groups,[41] the inherent steric hindrance of the lamellar bilayer m-A(14) mono-amidosil inhibits the C=O coordination from leading to a lower number of C=O first ligands, relative to the situation found in the amorphous m-A(8) host.

4. Experimental Section

General Instrumentation: ^{29}Si MAS and ^{13}C CP/MAS NMR spectra were recorded with a Bruker Avance 400 (9.4 T) spectrometer at 79.49 and 100.62 MHz, respectively. ^{29}Si MAS NMR spectra were recorded with 2 μs ($\theta \approx 30°$) rf pulses, a recycle delay of 60 s and at a 5.0 kHz spinning rate. ^{13}C CP/MAS NMR spectra were recorded with 4 μs ^1H 90° pulses, 2 ms contact time, a recycle delay of 4 s and at a spinning rate of 8 kHz. Chemical shifts (δ) are quoted in ppm from TMS. The XRD patterns were recorded with a Philips X′Pert MPD powder X-ray diffractometer with monochromated Cu-K_α radiation (1.54 Å) in a 2θ range between 1 and 60° with a step of 0.05° and a resolution of 40 s per step. The Eu and Si content were obtained by ICP–OES (inductively coupled plasma optical emission spectroscopy) analysis on an Jobin Yvon Activa instrument with a glass concentric nebulizer. For the Eu analysis, the samples were digested under microwave irradiation with HCl (6 mL), HNO_3 (2 mL) and HF (1 mL) at 150 °C and dried. The F^- ion was removed by two successive additions of HCl (5 mL) after the evaporation. The solution was recovered in 20% HNO_3 (10 mL) and diluted. For the Si analysis, the samples were digested under microwave irradiation with HCl (6 mL), HNO_3 (2 mL) and HF (1 mL) and diluted. The method is accurate within 10%. FTIR spectra were acquired at room temperature by using a Bruker 22 (Vektor) spectrometer placed inside a glove box with a dry argon atmosphere. The spectra were collected over the 4000–400 cm^{-1} range by averaging 150 scans at a spectral resolution of 2 cm^{-1}. Solid samples (2 mg) were finely ground, mixed with approximately 175 mg of dried potassium bromide (Merck, spectroscopic grade) and pressed into pellets. Prior to recording the spectra, the pellets were first vacuum dried at 80–90 °C for about 60 h, in order to reduce the levels of adsorbed water and solvent, and then transferred into a glove box. To evaluate complex band FTIR envelopes and to identify underlying spectral components, the iterative least-squares curve-fitting procedure in the PeakFit[47] software was used extensively throughout this study. The best fit of the experimental data was obtained by varying the frequency, bandwidth and intensity of the bands. Taking into account the morphology of materials under investigation, we decided to employ Voight band shapes. A linear baseline correction with a tolerance of 0.2% was employed. The standard errors of the curve-fitting procedures were less than 0.02. Differential scanning calorimetry measurements were obtained with a DSC131 Setaram DSC. A mass of approximately 10 mg was placed in 40 μL aluminium cans and stored in a desiccator over phosphorus pentoxide for one week at room temperature under vacuum. After the drying treatment, the cans were hermetically sealed, and the thermograms were recorded. Each sample was heated from 20 to 300 °C at 10 °C min^{-1}. The purge gas used in all experiments was purity nitrogen (N_2) supplied at a constant flow rate of 35 $cm^3 min^{-1}$. The photoluminescence and lifetime measurements were recorded with a Fluorolog®-3 (FL3–2T model) spectrometer with double excitation, fitted with a 1200 grooves/mm grating blazed at 330 nm, and a single-emission spectrometer (TRIAX 320), fitted with a 1200 grooves/mm grating blazed at 500 nm, coupled to a R928 photomultiplier. The excitation sources were a 450 W Xe arc lamp and a pulsed Xe-Hg lamp (6 μs pulse at half width and 20–30 μs tail) for the steady-state and time-resolved measurements, respectively. Excitation spectra were corrected from 240 to 600 nm for the spectral distribution of the

lamp intensity by using a photodiode reference detector. Emission spectra were also corrected for the spectral response of the monochromators and the detector by using typical correction spectra provided by the manufacturer. The absolute emission quantum yields were measured at room temperature by using a quantum yield measurement system (C9920–02 from Hamamatsu) with a 150 W Xe lamp coupled to a monochromator for wavelength discrimination, an integrating sphere as sample chamber and a multichannel analyzer for signal detection. Three measurements were made for each sample and the average value was reported. The method is accurate to within 10%.

Supporting Information (see footnote on the first page of this article): Details of synthesis, ^{13}C CP/MAS and ^{29}Si MAS NMR, XRD, TGA, FTIR data, emission and excitation spectra as a function of temperature, salt concentration and pendant alkyl chain size.

Acknowledgments

This work was supported by the Fundação para a Ciência e Tecnologia and FEDER (PTDC/CTM/72093/2006). S. C. N. acknowledges the Fundação para a Ciência e Tecnologia (SFRH/BPD/63152/2009), and J. P. thanks the Spanish Ministerio de Ciencia e Innovación (FPU fellowship). The authors are grateful to Denis Ostrovskii of the Department of Applied Physics, Chalmers University of Technology, Göteborg, Sweden, for recording the FT-IR and FT-Raman spectra.

[1] C. J. Brinker, G. Scherer W. *Sol–Gel Science: The Physics and Chemistry of Sol–Gel Processing*, Academic Press, San Diego, CA, **1990**.
[2] P. Gomez-Romero, C. Sanchez (Eds.), *Functional Hybrid Materials*, Wiley Interscience, New York, **2003**.
[3] C. Sanchez, B. Julián, P. Belleville, M. Popall, *J. Mater. Chem.* **2005**, *15*, 3559–3592.
[4] C. T. Kresge, M. E. Leonowicz, W. J. Roth, J. C. Vartulli, J. S. Beck, *Nature* **1992**, *359*, 710–712.
[5] Q. Huo, D. I. Margolese, U. Ciesla, P. Fena, T. E. Gier Sieger, P. R. Leon, P. M. Petroff, F. Schuth, G. D. Stucky, *Nature* **1994**, *368*, 317–321.
[6] Y. Lu, R. Ganguli, C. A. Drewien, M. T. Anderson, C. J. Brinker, W. Gong, Y. Guo, H. Soyez, B. Dunn, M. H. Huang, J. I. Zink, *Nature* **1997**, *389*, 364–368.
[7] C. J. Brinker, Y. F. Lu, A. Sellinger, H. Y. Fan, *Adv. Mater.* **1999**, *11*, 579–585.
[8] C. Bied, D. Gauthier, J. J. E. Moreau, M. Wong Chi Man, *J. Sol–Gel Sci. Technol.* **2001**, *20*, 313–320.
[9] S. Inagaki, S. Guan, T. Ohsuna, O. Terasaki, *Nature* **2002**, *416*, 304–307.
[10] a) J. J. E. Moreau, L. Vellutini, M. Wong Chi Man, C. Bied, J.-L. Bantignies, P. Dieudonne, J.-L. Sauvajol, *J. Am. Chem. Soc.* **2001**, *123*, 7957–7958; b) J. E. Moreau, L. Vellutini, M. W. Chi Man, C. Bied, *Chem. Eur. J.* **2003**, *9*, 1594; c) J. J. E. Moreau, B. P. Pichon, M. Wong Chi Man, C. Bied, H. Pritzkow, J. L. Bantignies, P. Dieudonné, J.-L. Sauvajol, *Angew. Chem. Int. Ed.* **2004**, *43*, 203–206; d) J. J. E. Moreau, L. Vellutini, M. Wong Chi Man, C. Bied, J.-L. Bantignies, J.-L. Sauvajol, *Chem. Eur. J.* **2005**, *11*, 1527–1537.
[11] A. N. Parikh, M. A. Schivley, E. Koo, K. Seshadri, D. Aurentz, K. Mueller, D. L. Allara, *J. Am. Chem. Soc.* **1997**, *119*, 3135–3143.
[12] a) A. Shimojima, Y. Sugahara, K. Kuroda, *Bull. Chem. Soc. Jpn.* **1997**, *70*, 2847–2853; b) Y. Fujimoto, A. Shimojima, K. Kuroda, *Chem. Mater.* **2003**, *15*, 4768–4774; c) A. Shimojima, K. Kuroda, *Angew. Chem. Int. Ed.* **2003**, *42*, 4057–4060.
[13] N. Liu, B. Smarsly, D. R. Dunphy, Y.-B. Jiang, C. J. Brinker, *J. Am. Chem. Soc.* **2002**, *124*, 14540–14541.
[14] B. Boury, R. J. P. Corriu, *Chem. Commun.* **2002**, 795–802.
[15] L. D. Carlos, V. de Zea Bermudez, V. S. Amaral, S. C. Nunes, N. J. O. Silva, R. A. Sá Ferreira, J. Rocha, C. V. Santilli, D. Ostrovskii, *Adv. Mater.* **2007**, *19*, 341–348.
[16] L. D. Carlos, R. A. S. Ferreira, V. de Zea Bermudez, S. J. L. Ribeiro, *Adv. Mater.* **2009**, *21*, 509–534.
[17] T. Zhang, S. Liu, D. G. Kurth, C. F. J. Faul, *Adv. Funct. Mater.* **2009**, *19*, 642–652.
[18] L. Sarakha, C. Forano, P. Boutinaud, *Opt. Mater. (Amsterdam)* **2009**, *31*, 562–566.
[19] S. S. Nobre, C. D. S. Brites, R. A. S. Ferreira, V. de Zea Bermudez, C. Carcel, J. J. Moreau, J. Rocha, M. W. Chi Man, L. D. Carlos, *J. Mater. Chem.* **2008**, *18*, 4172–4182.
[20] S. C. Nunes, PhD Dissertation, Vila Real, Portugal, **2008**, 92678/1/2 SD (http://opac.sde.utad.pt/geral/).
[21] Y. Fan, M. Kobayashi, H. Kise, *J. Polym. Sci., Part A: Polym. Chem.* **2001**, *39*, 1318–1328.
[22] S. Stevelmans, J. C. M. van Hest, J. F. G. A. Jansen, D. A. F. J. van Boxtel, E. M. M. de Brabander-van den Berg, E. W. Meijer, *J. Am. Chem. Soc.* **1996**, *118*, 7398–7399.
[23] C. Arenz, A. Giannis, *Eur. J. Org. Chem.* **2001**, 137–140.
[24] M. Pursch, A. Jäger, T. Schneller, R. Brindle, K. Albert, E. Lindner, *Chem. Mater.* **1996**, *8*, 1245–1252.
[25] L.-Q. Wang, J. Liu, G. J. Exarhos, K. Y. Flanigan, R. Bordia, *J. Phys. Chem. B* **2000**, *104*, 2810–2816.
[26] J. Clauss, K. Schmidt-Rohr, A. Adam, C. Boeffel, H. W. Spiess, *Macromolecules* **1992**, *25*, 5208–5214.
[27] L. D. Carlos, V. de Zea Bermudez, R. A. Sá Ferreira, L. Marques, M. Assunção, *Chem. Mater.* **1999**, *11*, 581–588.
[28] C. Bohm, F. Leveiller, D. Jacquemain, H. Mohwald, K. Kjaer, J. Als-Nielsen, I. Weissbuch, L. Leiserowitz, *Langmuir* **1994**, *10*, 830–836.
[29] J. F. Nagle, M. Goldstein, *Macromolecules* **1985**, *18*, 2643.
[30] R. G. Snyder, H. L. Strauss, C. A. Ellinger, *J. Phys. Chem.* **1982**, *86*, 5145–5150.
[31] T. Miyazawa, T. Shimanouchi, S.-I. Mizushima, *J. Chem. Phys.* **1956**, *24*, 408–418.
[32] a) D. J. Skrovanek, S. E. Howe, P. C. Painter, M. M. Coleman, *Macromolecules* **1985**, *18*, 1676–1683; b) D. J. Skrovanek, P. C. Painter, M. Coleman, *Macromolecules* **1986**, *19*, 699–705; c) M. M. Coleman, K. H. Lee, D. J. Skrovanek, P. C. Painter, *Macromolecules* **1986**, *19*, 2149–2157.
[33] Å. Wendsjö, J. Lindgren, J. O. Thomas, G. C. Farrington, *Solid State Ionics* **1992**, *53–56*, 1077–1082.
[34] A. Bernson, J. Lindgren, *Solid State Ionics* **1993**, *60*, 31–36.
[35] G. Petersen, A. Brodin, L. M. Torell, M. J. Smith, *Solid State Ionics* **1994**, *72*, 165–171.
[36] S. Chintapalli, C. Quinton, R. Frech, C. A. Vincent, *Macromolecules* **1997**, *30*, 7472–7477.
[37] V. de Zea Bermudez, D. Ostrovskii, S. Lavoryk, M. C. Gonçalves, L. D. Carlos, *Phys. Chem. Chem. Phys.* **2004**, *6*, 649–658.
[38] a) L. D. Carlos, R. A. Sá Ferreira, V. de Zea Bermudez, S. J. L. Ribeiro, *Adv. Funct. Mater.* **2001**, *2*, 111–115; b) L. D. Carlos, R. A. Sá Ferreira, R. N. Pereira, M. Assunção, V. de Zea Bermudez, *J. Phys. Chem. B* **2004**, *108*, 14924–14932; c) S. S. Nobre, P. P. Lima, L. Mafra, R. A. S. Ferreira, R. Freire, L. Fu, U. Pischel, V. de Zea Bermudez, O. L. Malta, L. D. Carlos, *J. Phys. Chem. C* **2007**, *111*, 3275–3284; d) S. C. Nunes, V. de Zea Bermudeza, J. Cybinska, R. A. S. Ferreira, J. Legendziewicz, L. D. Carlos, M. M. Silva, M. J. Smith, D. Ostrovskii, J. Rocha, *J. Mater. Chem.* **2005**, *15*, 3876–3886.
[39] P. P. Lima, S. S. Nobre, R. O. Freire, S. A. Júnior, R. A. S. Ferreira, U. Pischel, O. L. Malta, L. D. Carlos, *J. Phys. Chem. C* **2007**, *111*, 17627–17634.
[40] R. A. S. Ferreira, L. D. Carlos, R. R. Gonçalves, S. J. L. Ribeiro, V. de Zea Bermudez, *Chem. Mater.* **2001**, *13*, 2991–2998.
[41] a) L. D. Carlos, R. A. S. Ferreira, V. D. Bermudez, C. Molina, L. A. Bueno, S. J. L. Ribeiro, *Phys. Rev. B* **1999**, *60*, 10042–

10053; b) L. D. Carlos, Y. Messaddeq, H. F. Brito, R. A. S. Ferreira, V. D. Bermudez, S. J. L. Ribeiro, *Adv. Mater.* **2000**, *12*, 594–598.
[42] a) C. W. Struck, W. H. Fonger, *J. Lumin.* **1970**, *1*, 456–469; b) C. W. Struck, W. H. Fonger, *J. Chem. Phys.* **1970**, *52*, 6364–6372.
[43] V. de Zea Bermudez, D. Ostrovskii, M. C. Gonçalves, S. Lavoryk, L. D. Carlos, R. A. S. Ferreira, *J. Phys. Chem. B* **2005**, *109*, 7110–7119.
[44] a) S. T. Frey, W. De Horrocks Jr., *Inorg. Chim. Acta* **1995**, *229*, 383–390; b) O. L. Malta, H. J. Batista, L. D. Carlos, *Chem. Phys.* **2002**, *282*, 21–30; L. D. Carlos, O. L. Malta, R. Q. Albuquerque, *Chem. Phys. Lett.* **2005**, *415*, 238–242.
[45] C. De Mello Donega, S. J. L. Ribeiro, R. R. Gonçalves, G. Blasse, *J. Phys. Chem. Solids* **1996**, *57*, 1727–1734.
[46] R. M. Supkowski, W. D. Horrocks, *Inorg. Chim. Acta* **2002**, *340*, 44–48.
[47] Peakfit, Jandel Corporation, 2591 Rerner Boulevard, San Rafael, CA 94901, U.S.A.

Received: February 10, 2010
Published Online: May 6, 2010

